Chem

Why sulfur is important in lincosamide antibiotics

Graphical abstract

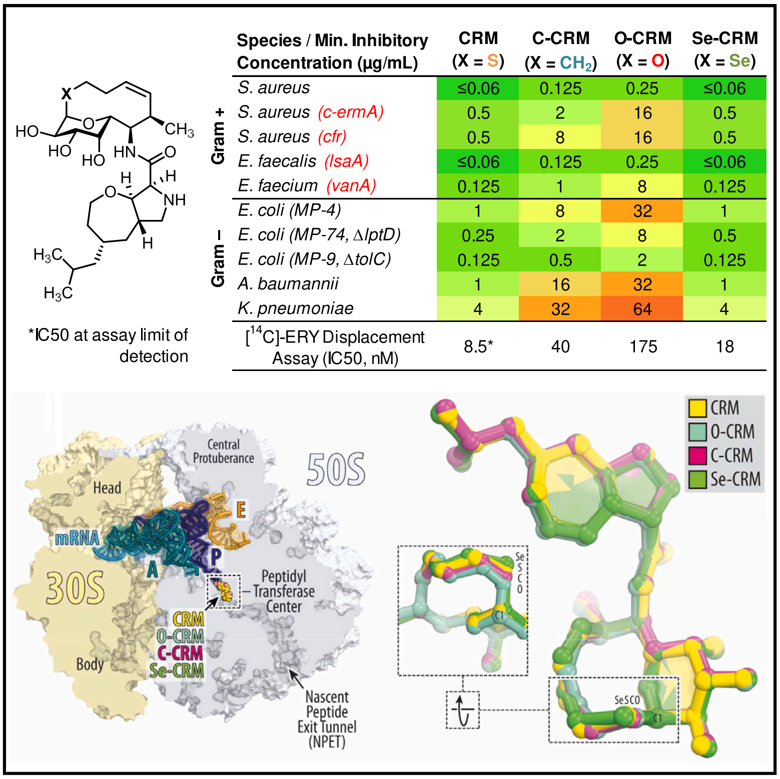

	Species / Min. Inhibitory Concentration (μg/mL)	CRM (X = S)	C-CRM (X = CH_2)	O-CRM (X = O)	Se-CRM (X = Se)
Gram +	*S. aureus*	≤0.06	0.125	0.25	≤0.06
	S. aureus (c-ermA)	0.5	2	16	0.5
	S. aureus (cfr)	0.5	8	16	0.5
	E. faecalis (lsaA)	≤0.06	0.125	0.25	≤0.06
	E. faecium (vanA)	0.125	1	8	0.125
Gram –	*E. coli (MP-4)*	1	8	32	1
	E. coli (MP-74, ΔlptD)	0.25	2	8	0.5
	E. coli (MP-9, ΔtolC)	0.125	0.5	2	0.125
	A. baumannii	1	16	32	1
	K. pneumoniae	4	32	64	4
	$[^{14}C]$-ERY Displacement Assay (IC50, nM)	8.5*	40	175	18

*IC50 at assay limit of detection

Highlights

- Sulfur replacement analogs (CH_2, O, Se) of the antibiotic cresomycin were synthesized
- Replacing the sulfur atom led to lower antibacterial activity or metabolic stability
- The sulfur atom engages rRNA nucleobase G2505 in an essential S-π interaction
- Structural, biochemical, and computational studies support S-π interaction hypothesis

Authors

Kelvin J.Y. Wu, Elena V. Aleksandrova,
Paul J. Robinson, ..., Joonho Lee,
Yury S. Polikanov, Andrew G. Myers

Correspondence

joonholee@g.harvard.edu (J.L.),
yuryp@uic.edu (Y.S.P.),
myers@chemistry.harvard.edu (A.G.M.)

In brief

We describe the chemical syntheses, MIC analyses, biochemical profiling, ribosome-bound X-ray crystal structures, and computational studies of cresomycin (CRM) sulfur atom replacement analogs C-CRM (S → CH_2), O-CRM (S → O), and Se-CRM (S → Se), making side-by-side comparisons with CRM. We show that the anomeric sulfur atom within lincosamide antibiotics participates in an essential S-π interaction with rRNA nucleobase G2505 and conclude that the sulfur atom is important for maintaining effective binding of the antibiotic to the bacterial ribosome.

Wu et al., 2025, Chem *11*, 102480
July 10, 2025
https://doi.org/10.1016/j.chempr.2025.102480

CellPress

Chem

CellPress

Article

Why sulfur is important in lincosamide antibiotics

Kelvin J.Y. Wu,[1,5] Elena V. Aleksandrova,[2,5] Paul J. Robinson,[1,5] Amy E. Benedetto,[1] Meiyi Yu,[1] Ben I.C. Tresco,[1] Dominic N.Y. See,[1] Tong Jiang,[1] Antonio Ramkissoon,[1] Clémence F. Dunand,[3,4] Maxim S. Svetlov,[3,4] Joonho Lee,[1,*] Yury S. Polikanov,[2,3,4,*] and Andrew G. Myers[1,6,*]

[1] Department of Chemistry and Chemical Biology, Harvard University, Cambridge, MA 02138, USA
[2] Department of Biological Sciences, University of Illinois at Chicago, Chicago, IL 60607, USA
[3] Department of Pharmaceutical Sciences, University of Illinois at Chicago, Chicago, IL 60607, USA
[4] Center for Biomolecular Sciences, University of Illinois at Chicago, Chicago, IL 60607, USA
[5] These authors contributed equally
[6] Lead contact
*Correspondence: joonholee@g.harvard.edu (J.L.), yuryp@uic.edu (Y.S.P.), myers@chemistry.harvard.edu (A.G.M.)

https://doi.org/10.1016/j.chempr.2025.102480

THE BIGGER PICTURE Lincosamide antibiotics, such as clindamycin, are rapidly degraded in animals and humans by hepatic sulfoxidation of their sulfur atom. Despite this known metabolic liability, all approved lincosamide antibiotics invariably conserve this sulfur atom; sulfur atom replacement analogs of extant lincosamides have been prepared in prior work but lacked the potent antibacterial activities of their sulfur-containing counterparts. This work confirms and explains the important role of the sulfur atom in the binding of lincosamide antibiotics to their target, the bacterial ribosome. Understanding the essential nature of the sulfur atom within the lincosamides will help direct future optimization efforts in this important class of antibiotics and potentially other therapeutics.

SUMMARY

We recently reported the conception and synthesis of cresomycin (CRM), a fully synthetic lincosamide antibiotic effective *in vitro* and *in vivo* against multidrug-resistant Gram-positive and Gram-negative bacteria. In this work, we describe the chemical synthesis and characterization of CRM sulfur atom replacement analogs C-CRM (S → CH_2), O-CRM (S → O), and Se-CRM (S → Se). Comparison of high-resolution co-crystal structures showed that all four analogs adopted identical conformations when bound to the bacterial ribosome, but due to variations of ≤ 1 Å in the bond lengths between the anomeric carbon and the varied atoms, only the S and Se heteroatoms of CRM and Se-CRM, respectively, were positioned to interact with the π-face of nucleobase G2505. C-CRM and O-CRM did not benefit from such stabilizations, with correspondingly negative consequences in both target engagement and antibacterial activities. We therefore conclude that the sulfur atom of the lincosamides is important in ribosomal binding.

INTRODUCTION

The bacterial ribosome translates bacterial nucleic acid information molecules (RNA) into protein readouts and is the primary target for multiple evolutionarily independent, structurally distinct classes of natural products with antibiotic activity.[1,2] The lincosamides form one such class of antibiotics and inhibit protein synthesis by binding to the peptidyl transferase center (PTC) within the large (50S) ribosomal subunit.[3] However, both of the two US Food and Drug Administration (FDA)-approved lincosamide antibiotics, lincomycin[4] (1964), and clindamycin[5] (CLI, 1970, Figure 1A), are rapidly cleared in animals and humans by hepatic sulfoxidation.[6,7] Recognizing the anomeric thioether group as a metabolic liability, researchers at Vicuron Pharmaceuticals[8] and, subsequently, our own laboratory,[9] employed chemical synthesis to prepare lincosamide sulfur atom replacement analogs, but invariably these analogs proved to be inferior antibiotic candidates in minimum inhibitory concentration (MIC) analyses, with no clear explanation as to why. With the recent discovery of the fully synthetic macrobicyclic oxepanoprolinamide antibiotic cresomycin (CRM, Figure 1A), which exhibits potent activity in both Gram-positive and Gram-negative bacterial strains, including those expressing one or more genes conferring antimicrobial resistance (AMR) to CLI and other antibiotics, we saw an opportunity to investigate in a new context atomic replacement of the anomeric sulfur atom of CRM, which like CLI undergoes hepatic sulfoxidation, albeit at a significantly slower rate.[10] In this work, we describe the chemical syntheses, MIC analyses, biochemical profiling, ribosome-bound X-ray crystal structures, and computational studies of CRM sulfur

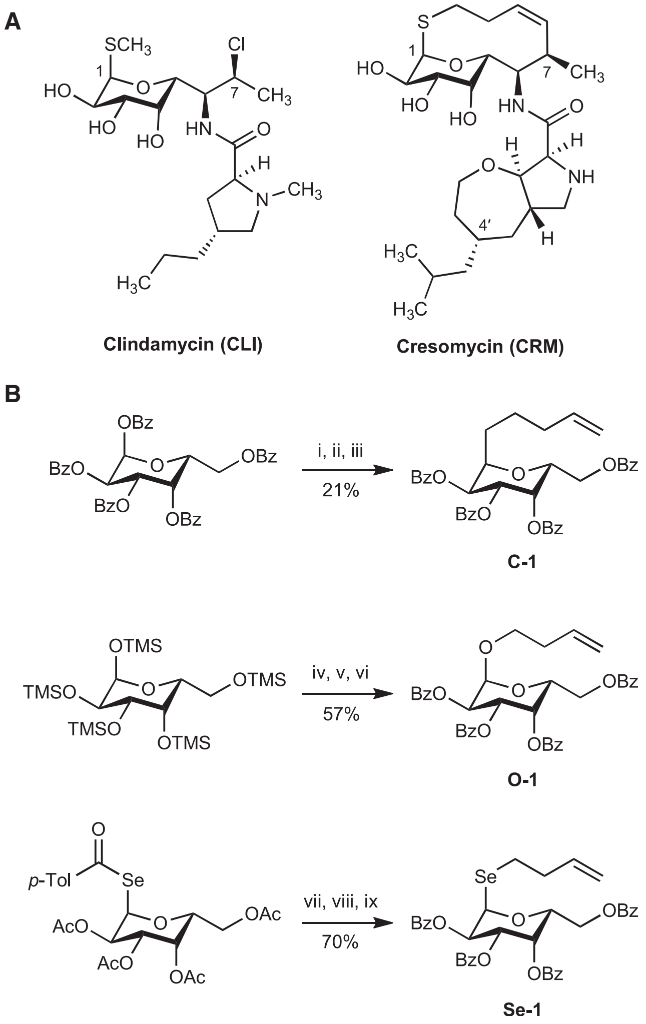

Figure 1. Representative lincosamide antibiotics and synthesis of sulfur atom replacement intermediates C-1, O-1, and Se-1

(A) Chemical structures of clindamycin (CLI) and cresomycin (CRM).

(B) Synthesis of perbenzoylated intermediates C-1, O-1, and Se-1.

Reagents and conditions: (1) allyltrimethylsilane, $BF_3 \cdot OEt_2$; (2) 9-BBN; (3) vinyl bromide, Cs_2CO_3, $Pd(dppf)Cl_2$; (4) TMSI, then 3-buten-1-ol, TBAI; (4) MeOH; (6) BzCl, pyridine; (7) 4-bromo-1-butene, piperazine, Cs_2CO_3; (8) NaOMe, MeOH; (9) BzCl, pyridine.

atom replacement analogs C-CRM (S → CH_2), O-CRM (S → O), and Se-CRM (S → Se), making side-by-side comparisons with CRM. The high-resolution crystal structures alongside antibacterial susceptibility measurements and computational analyses reveal why sulfur is important in targeting the bacterial ribosome.

RESULTS AND DISCUSSION

Synthesis of CRM sulfur atom replacement analogs

The three CRM sulfur atom replacement analogs C-CRM, O-CRM, and Se-CRM were synthesized by routes that paralleled the discovery synthetic route to CRM, each featuring a tactical two-step sequence of low-temperature (−108°C) crotylation of Ellman sulfinimine intermediates followed by a (*Z*)-selective ring-closing metathesis reaction using the Grubbs II catalyst.[10] The C-, O-, and Se-glycosidic precursors C-1, O-1, and Se-1, respectively, were prepared in three steps each from known α-D-galactose derived precursors, as depicted in Figure 1B. Thus, per-*O*-benzoylated α-D-galactopyranose[11] underwent α-selective *C*-allylation upon exposure to allyltrimethylsilane and boron trifluoride etherate[12]; the product was then treated with 9-borabicyclo[3.3.1]nonane (9-BBN) and the resultant trialkylborane intermediate was subjected to *B*-alkyl Suzuki coupling with bromoethylene to furnish C-1 in 21% yield for the three-step sequence. Per-*O*-trimethylsilylated α-D-galactopyranose[13] underwent α-selective *O*-glycoside formation with trimethylsilyl iodide (TMSI) and 3-buten-1-ol in the presence of tetrabutylammonium iodide[14] (TBAI); the product was then subjected to global silyl deprotection and benzoyl reprotection to furnish O-1 in 57% yield for the three-step sequence. Per-*O*-acetylated *p*-toluoyl α-D-selenogalactopyranoside[15] underwent *Se*-alkylation with 4-bromo-1-butene in the presence of piperazine and cesium carbonate[15]; the product was then subjected to global acetate deprotection and benzoyl reprotection to furnish **Se-1** in 70% yield for the three-step sequence.

Intermediates C-1, O-1, and Se-1 were transformed via identical reaction sequences to afford C-CRM, O-CRM, and Se-CRM, respectively; as a representative example, the full synthetic sequence for the specific instance of C-CRM is illustrated in Figure 2A. In brief, selective deprotection of the primary benzoyl group within C-1, followed by oxidation of the resulting primary alcohol with the Dess-Martin periodinane (DMP) and condensation of the resultant aldehyde with (*R*)-*tert*-butylsulfinamide afforded the Ellman sulfinimine C-2 in 38% yield over three steps. Zinc-mediated crotylation of C-2 and subsequent Grubbs ring-closing metathesis afforded the (*Z*)-macrobicycle C-3 in 44% yield over two steps. Global benzoyl and sulfinamide deprotection gave the macrobicyclic amine C-4 in 36% yield over the two steps. Last, amide coupling of C-4 with the oxepanoproline southern fragment (1)[16,17] followed by *N*-Boc deprotection afforded C-CRM in 44% yield over the two steps. The sulfur atom replacement analogs O-CRM (Figure 2B) and Se-CRM (Figure 2C) were prepared in analogous fashion; all three analogs were prepared in amounts sufficient for antimicrobial and biochemical profiling (>5 mg). Their proton nuclear magnetic resonance (^1H NMR) spectra were remarkably similar to those of CRM (see supplemental information), which suggested that the conformations of the atomic replacement analogs were similar to CRM, a proposal that was borne out in X-ray crystallographic studies (*vide infra*).

Antimicrobial and biochemical profiling of CRM, C-CRM, O-CRM, and Se-CRM

CRM, C-CRM, O-CRM, and Se-CRM were evaluated in broth microdilution antimicrobial analyses using a panel of Gram-positive and Gram-negative bacteria (Figure 3). The single-atom substitution of sulfur in CRM for CH_2 (C-CRM) or oxygen (O-CRM) led to precipitous declines in antibacterial activity against all bacterial strains assessed. In contrast, the single-atom substitution of sulfur in CRM for selenium (Se-CRM) produced virtually no change in antibacterial activity against the same panel of

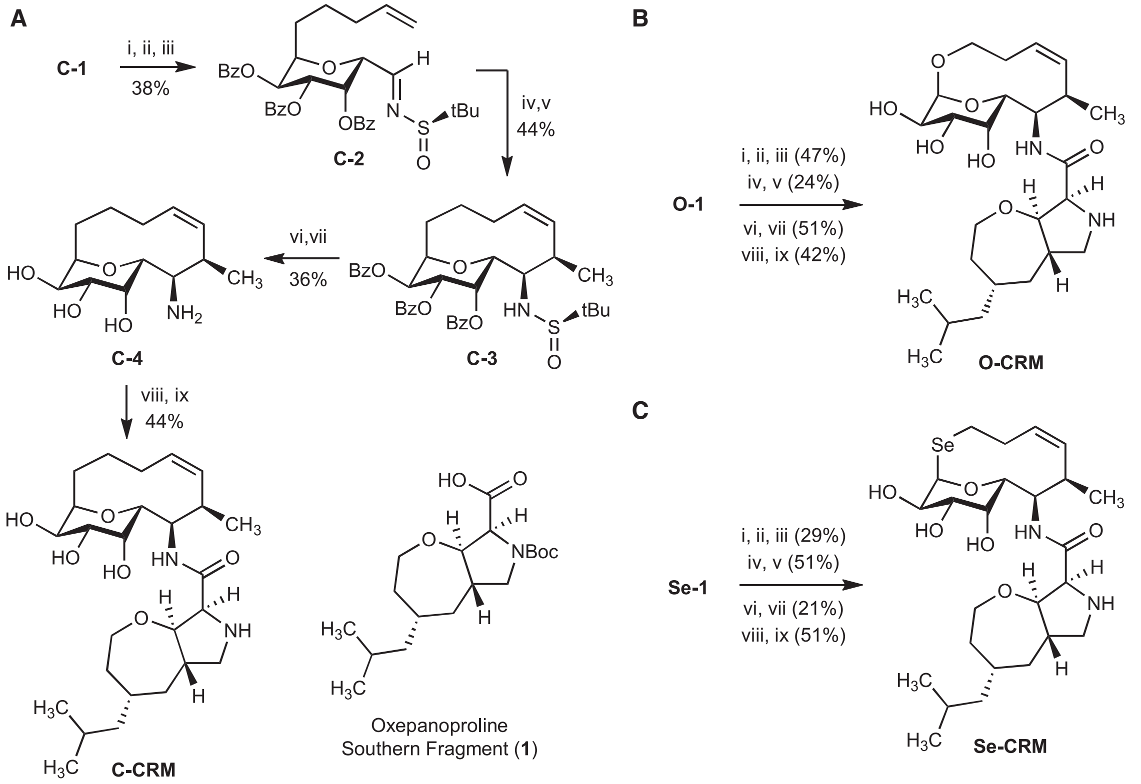

Figure 2. Synthesis of sulfur atom replacement analogs of CRM (C-CRM, O-CRM, and Se-CRM)

(A) Synthesis of C-CRM from intermediate C-1.

(B) Synthesis of O-CRM from intermediate O-1.

(C) Synthesis of Se-CRM from intermediate Se-1.

Reagents and conditions: (1) [*t*-$Bu_2Sn(OH)Cl]_2$, MeOH-THF; (2) DMP; (3) (*R*)-(+)-*t*-butylsulfinamide, $CuSO_4$; (4) crotyl chloride, Zn, LiCl, −108°C; (5) Grubbs II catalyst, 110°C; (6) NaOMe, MeOH; (7) HCl, dioxane; (8) oxepanoproline southern fragment (1), HATU, DIPEA; (9) HCl, dioxane-MeOH. Abbreviations: HATU, 1-[bis(dimethylamino)methylene]-1*H*-1,2,3-triazolo[4,5-*b*]pyridinium 3-oxide hexafluorophosphate; DIPEA, *N,N*-diisopropylethylamine.

isolates. When assessed in a human liver microsomal stability assay (Figures 3 and S1; Table S1), the half-life of O-CRM (119.9 min) was more than double the half-life of CRM (55.6 min) and more than quadruple the half-life of Se-CRM (27.2 min), highlighting a trend of decreased metabolic stability upon descension of the periodic table (from O to S to Se). The half-life of C-CRM in the presence of human liver microsomes (61.8 min) was only slightly longer than that of CRM (55.6 min). Interestingly, the only sulfur atom replacement analog that exhibited a marked improvement in metabolic stability (O-CRM) also showed the steepest decline in observed antibacterial activity.

To confirm that all four antibiotics (CRM, C-CRM, O-CRM, and Se-CRM) functioned by inhibiting the initiation of bacterial translation, we conducted primer extension inhibition ("toeprinting") analysis[18] upon all four molecules, the results of which strongly supported that conjecture (Figure S2). The antibacterial activity of an antibiotic targeting the bacterial ribosome can be viewed as a function of its membrane permeability, susceptibility to efflux, and target engagement.[19] To elucidate the mechanistic underpinnings behind the improved antibacterial activities of CRM and Se-CRM compared with C-CRM and O-CRM, we first evaluated the effect of efflux on Gram-negative antibacterial activity using the efflux ratio, determined by dividing each antibiotic's MIC against the wild-type *E. coli* strain (MP-4) by its MIC against an isogenic *E. coli* strain (MP-9) with loss-of-function mutations in the major efflux transporter gene (*tolC*). CRM, C-CRM, O-CRM, and Se-CRM displayed similar efflux ratios ranging from 8 to 16 (Figure 3), suggesting that the driver of antibacterial activity for CRM was not efflux avoidance. Next, we evaluated the effect of outer-membrane permeability on Gram-negative antibacterial activity using the permeability ratio, determined by dividing each antibiotic's MIC against the Δ*tolC E. coli* strain (MP-9) by its MIC against a hyperpermeable *E. coli* strain (MP-74) with a loss-of-function mutation in the outer-membrane assembly gene (*lptD*). CRM, C-CRM, O-CRM, and Se-CRM displayed similar permeability ratios ranging from 0.25 to 0.5 (Figure 3), suggesting that the driver of antibacterial activity for CRM was not membrane permeability. Last, the impact of target engagement was assessed, albeit indirectly, by measuring the concentrations necessary for each molecule to displace 50% of bound [^{14}C]-radiolabeled erythromycin from purified *E. coli* 70S ribosomes (IC_{50}) following literature precedent,[20] with results rank-ordered from lowest to highest required concentrations as follows

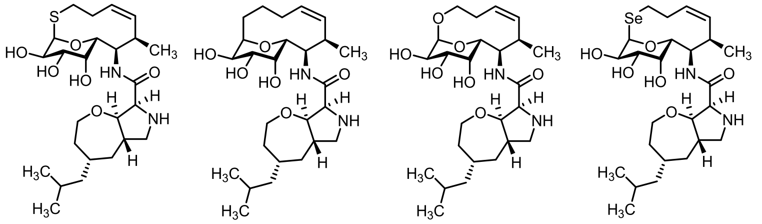

	Species	Strain Description	CRM	C-CRM	O-CRM	Se-CRM
Gram +	*S. aureus*	ATCC 29213	≤0.06	0.125	0.25	≤0.06
	S. aureus	*c-ermA*	0.5	2	16	0.5
	S. aureus	*cfr*	0.5	8	16	0.5
	E. faecalis	ATCC 29212, *lsaA*	≤0.06	0.125	0.25	≤0.06
	E. faecium	*vanA*	0.125	1	8	0.125
Gram –	*E. coli*	MP-4, ATCC 25922	1	8	32	1
	E. coli	MP-74, Δ*lptD*	0.25	2	8	0.5
	E. coli	MP-9, Δ*tolC*	0.125	0.5	2	0.125
	A. baumannii	ATCC 19606	1	16	32	1
	K. pneumoniae	FQ-R	4	32	64	4
	Human Hepatic Microsomal Stability ($T_{1/2}$, min)		55.6	61.8	119.9	27.2
	Efflux Ratio (MP-4 MIC / MP-9 MIC)		8	16	16	8
	Permeability Ratio (MP-9 MIC / MP-74 MIC)		0.5	0.25	0.25	0.25
	[^{14}C]-ERY Displacement Assay (IC50, nM)		8.5*	40	175	18

Figure 3. *In vitro* efficacies, metabolic profiling, and ribosomal displacement assays of CRM, C-CRM, O-CRM, and Se-CRM

Minimum inhibitory concentrations ($\mu g \cdot mL^{-1}$) against a panel of Gram-positive and Gram-negative pathogens, human liver microsomal stabilities (reported as half-lives in min, $T_{1/2}$), and competitive displacement assays with [^{14}C]-labeled erythromycin (reported as IC_{50}s in nM) for CRM, C-CRM, O-CRM, and Se-CRM. Abbreviations; *c-ermA*, constitutively expressed erythromycin rRNA methyltransferase A; *cfr*, chloramphenicol-florfenicol resistance methyltransferase; *lsaA*, ATP-binding cassette F (ABC-F) resistance protein; *vanA*, vancomycin-resistance gene; *tolC*, major efflux transporter gene; *lptD*, outer-membrane assembly gene; FQ-R, fluoroquinolone-resistant. *IC_{50} at assay limit of detection.

(Figures 3 and S3): CRM (8.5 nM, the lower limit of detection of the assay), Se-CRM (18 nM), C-CRM (40 nM), and O-CRM (175 nM). These findings correlate qualitatively with the measured MIC values of the antibiotics in both Gram-positive and Gram-negative bacterial strains, suggesting that the primary driver of antimicrobial activity in this series is target engagement.

Structural basis for differential target engagement by CRM sulfur atom replacement analogs

To gain further insights into the details of target engagements, we determined X-ray crystal structures of C-CRM, O-CRM, and Se-CRM in complex with *Thermus thermophilus* (*Tth*) 70S ribosomes at 2.50-Å, 2.50-Å, and 2.45-Å resolution, respectively (Figures 4 and S4; Table S2). As in the reported crystal structure of CRM bound to the *Tth* 70S ribosome,[10] all three crystal structures of the sulfur atom replacement analogs comprised identically bound mRNA, deacylated $tRNA^{Phe}$ in the A and E sites, and aminoacylated fMet-$tRNA_i^{Met}$ in the P site (Figure 4A). The Fourier difference maps that were obtained for C-CRM, O-CRM, and Se-CRM crystal structures revealed strong positive electron density, allowing us to determine unambiguously each of their structures (Figure S4). The binding sites of C-CRM, O-CRM, and Se-CRM are nearly indistinguishable from that of CRM and reside at the PTC of the *Tth* 70S ribosome (Figure S5A). In the southern hemisphere of all four antibiotics, the C4′-isobutyl group firmly engages the PTC by extending deep into the A-site cleft, occupying a hydrophobic pocket formed by the nucleobases A2451, C2452, and U2506 of the 23S rRNA (Figure S5B). This pocket normally accommodates the α-side chains of incoming aminoacyl tRNAs and plays a key role in positioning the aminoacylated 3′ end of A-site tRNA within the PTC during transpeptidation.[21,22] In the northern hemisphere, the macrobicyclic fragment of each atomic replacement analog is anchored identically in the PTC by an extensive network of hydrogen bonds with nucleotides A2058, A2059, and A2503 of the 23S rRNA (Figures S5C and S5D).

An overlay of the structures of CRM, C-CRM, O-CRM, and Se-CRM showed that the four macrobicyclic rings were essentially identical conformationally, but revealed subtle differences in the positions of the S, C, O, and Se atoms, respectively, relative to the π-face of nucleobase G2505 (Figure 4). The positions of these atoms are largely determined by the different lengths of their bonds to the anomeric carbon (C1, Figure 4B). For example, for O-CRM, the C1–O bond length was 1.44 Å and the oxygen atom was 3.90 Å away from the closest atom (C4) of G2505. For C-CRM, the C1–C bond length was 1.56 Å and the carbon atom was 3.76 Å from C4 of G2505. For CRM, the C1–S bond length was 1.81 Å and the sulfur atom was 3.43 Å from C4 of G2505. For Se-CRM, the C1–Se bond length was 2.00 Å and the selenium atom was 3.34 Å from C4 of G2505. These observations support the hypothesis that CRM ribosomal binding benefits from an S-π interaction with nucleobase G2505 and explain the different ribosomal binding affinities of each atomic replacement analog. Thus, the sulfur and selenium atoms of CRM and Se-CRM, respectively, are sufficiently diffuse and well-positioned (by virtue of their longer C1–S and C1–Se bond lengths)

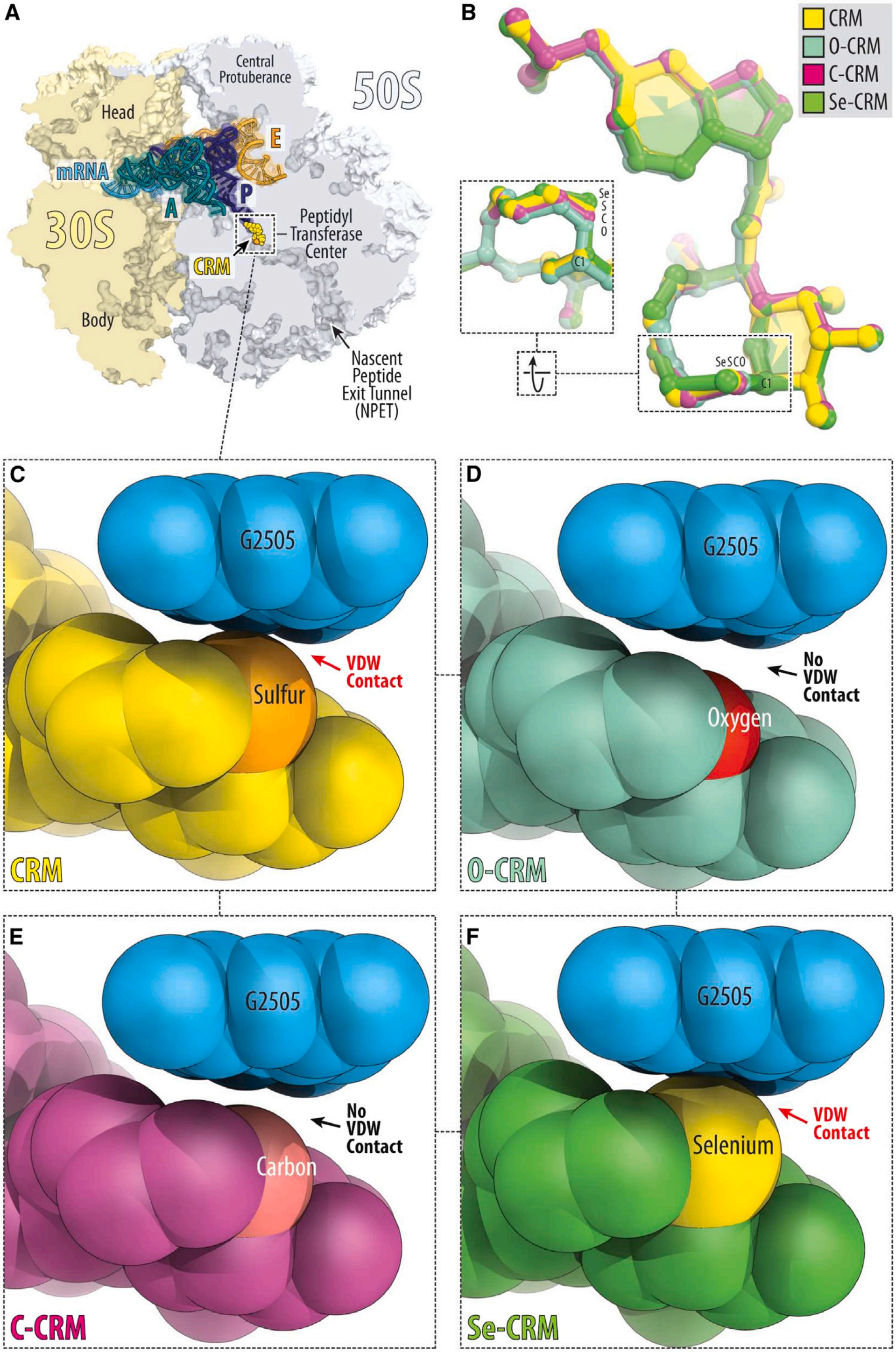

Figure 4. Structures of CRM, C-CRM, O-CRM, and Se-CRM in complex with the bacterial ribosome

(A) Overview of the binding site for CRM (yellow, PDB: 8UD6) in the PTC of the 70S ribosome showing the 30S subunit (light yellow), the 50S subunit (light blue), A-site tRNA (teal), P-site tRNA (navy), E-site tRNA (orange), and mRNA (blue).

(B) Superposition of the structures of CRM and its sulfur atomic replacement analogs bound to the *T. thermophilus* 70S ribosome. All structures were aligned based on domain V of the 23S rRNA.

(C–F) Close-up views of the ribosome-bound antibiotics comparing the VDW contacts of the sulfur atom (CRM, C), oxygen atom (O-CRM, D), CH_2 group (C-CRM, E), and selenium atom (Se-CRM, F) with the π-face of nucleobase G2505 of the 23S rRNA. Note that only the sulfur and selenium atoms are sufficiently diffuse and close to nucleobase G2505 to engage in productive VDW interactions.

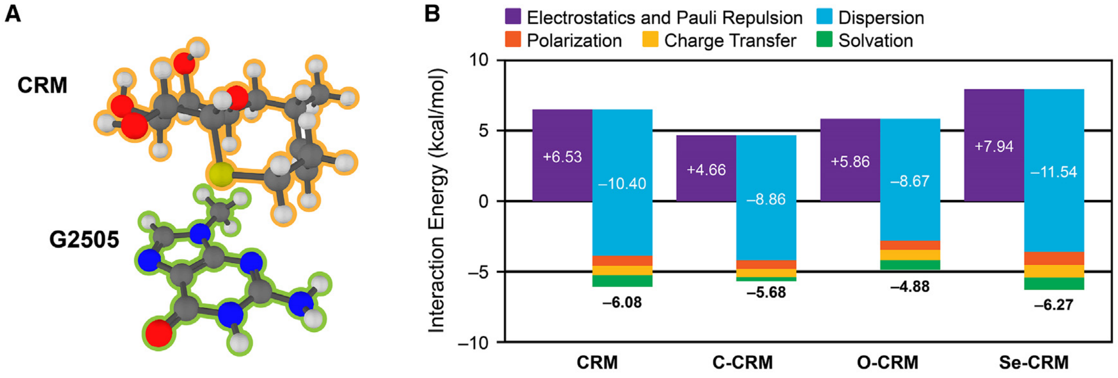

Figure 5. Computational study of the interaction energy between the nucleobase G2505 and CRM and its sulfur atom replacement analogs

(A) Representative fragment model of nucleobase G2505 (green outline) and CRM (orange outline).

(B) Energy decomposition analyses of the interaction energies of CRM, C-CRM, O-CRM, and Se-CRM. Note that in all cases, the dispersion force is the largest stabilizing interaction.

to engage with the π-face of G2505. In contrast, the more compact van der Waals (VDW) atomic radius and the shorter C1–O bond length of O-CRM place the oxygen atom too far away from G2505 to engage in an O-π interaction. Last, unlike the chalcogen-containing analogs, the anomeric methylene group of C-CRM has no lone-pair electrons to interact with G2505.

Theoretical support for an S-π interaction in CRM ribosomal binding

To better understand the role of the sulfur atom of CRM relative to its atomic replacement analogs in ribosomal binding, we applied density functional theory (DFT) to assess the interaction energies of CRM and each sulfur atom replacement analog with the nucleobase G2505 using the minimal fragment model depicted in Figure 5A.[23] The DFT analyses were performed using the reported continuum dielectric constant of DNA ($\varepsilon = 8.00$) to approximate the rRNA microenvironment[24] and were validated using the auxiliary-field quantum Monte Carlo[25,26] (AFQMC) method (Figure S6). The DFT calculations (Figure 5B) showed that O-CRM had the weakest interaction energy with G2505 (−4.88 kcal/mol), followed by C-CRM (−5.68 kcal/mol), CRM (−6.08 kcal/mol), then Se-CRM (−6.27 kcal/mol). Energy decomposition analysis was performed using the absolutely localized molecular orbitals (ALMO-EDA) technique,[23] which revealed that dispersion forces provided the primary attractive interaction for CRM and each sulfur atom replacement analog, and were weakest for O-CRM (−8.67 kcal/mol), followed by C-CRM (−8.86 kcal/mol), CRM (−10.40 kcal/mol), then Se-CRM (−11.54 kcal/mol), in accord with the structural and microbiological data presented above.

Conclusions

The structurally distinct lincosamide natural products lincomycin and celesticetin[27] (Figure S7), produced by different strains of *Streptomyces* using evolutionarily distinct biosynthetic pathways, are notably variant in both the northern and southern hemispheres, yet both retain a common anomeric sulfur atom as part of different thioether linkages. All semisynthetic lincosamide antibiotics approved for human (CLI, Figure 1A) or veterinary (pirlimycin,[28] Figure S7) medicine similarly retain an anomeric thioether substituent, in spite of efforts to replace this group, as discussed above. The high-resolution ribosomal crystal structures reported herein, supported by state-of-the-art computational studies, make evident the importance of VDW stabilization between the sulfur atom of CRM and the π-face of nucleobase G2505.[3] The selenium atom of Se-CRM benefits from a similar stabilization upon ribosomal binding and displays MIC values in antibacterial screening that are nearly indistinguishable from those of CRM, but Se-CRM also displayed the shortest half-life (27.2 min) in the presence of human liver microsomes, which was perhaps to be expected. Apart from a remarkable atomic-level analysis of ribosomal binding by a series of PTC-targeting antibiotics, a daunting conclusion from inspection of the MIC table of Figure 3 is the extraordinary sensitivity of antibacterial activities to structural perturbations arising from atomic variations that produce changes in bond lengths of less than an angstrom. Though we now view the sulfur atom of lincosamide antibiotics as essential, the anomeric thioether remains a metabolic liability *in vivo*; we have therefore employed strategies other than atomic replacement to attenuate hepatic oxidation. These include steric occlusion of the sulfur atom, as in CRM, and judicious placement of electron-withdrawing fluorine atoms near the sulfur atom, as in the antibiotic candidate BT-33.[29]

METHODS

Antibacterial susceptibility testing

In vitro antibiotic susceptibility testing was performed using the broth microdilution method in accordance with the Clinical and Laboratory Standards Institute (CLSI) guidelines.[30] The chemical syntheses of C-CRM, O-CRM, and Se-CRM, alongside their associated NMR spectra, are outlined in the supplemental information. CRM was synthesized according to literature precedent.[10] All test compounds were stored as dry powders at −20°C prior to use. Working solutions of test compounds were made at a concentration of 3.2 $\text{mg}\cdot\text{mL}^{-1}$ in dimethyl sulfoxide (DMSO) immediately before use. Final antibiotic concentrations ranged from 32 to 0.06 $\mu g \cdot mL^{-1}$, in steps of 2-fold dilutions, and maintained a final DMSO concentration of 2%.

Bacterial isolates were obtained from the American Type Culture Collection (ATCC; Manassas, VA, USA), JMI Laboratories (North Liberty, IA, USA), Micromyx repository (MMX; Kalamazoo, MI, USA), or Massachusetts Eye and Ear (Boston, MA, USA). All isolates were cryopreserved at −80°C in glycerol stocks (20% glycerol in species-specific media). All isolates were revived from cryopreservation and sub-cultured on brain heart infusion agar (BD Diagnostics; Sparks, MD, USA) at 37°C in 5% CO_2 for 24 h prior to experimentation.

For all organisms, 3–5 uniform colonies were picked from subcultures and suspended in 10 mL of cation-adjusted Mueller Hinton broth (ca-MHB) and incubated for 2–3 h at 37°C while being shaken at 250 rpm. The bacterial suspensions were then adjusted to a 0.5 MacFarland standard and further diluted 1:200 in ca-MHB to obtain a final test inoculum of 5×10^5 CFU mL^{-1}. 96-well plates were seeded with DMSO solutions of the test compounds in a 2-fold serial dilution series. The final test inoculum of each organism in ca-MHB was then added and the plates were incubated for 18–24 h at 37°C. MIC values were represented as the modal value of biological triplicate experiments.

Hepatic microsomal stability

Hepatic microsomal stability was evaluated by incubating 1 μM of CRM, C-CRM, O-CRM, or Se-CRM with 1 mg/mL human hepatic microsomes in 100 mM potassium phosphate buffer at pH 7.4. The reaction was initiated by adding nicotinamide adenine dinucleotide phosphate (NADPH) to achieve a final concentration of 1 mM. Aliquots were removed at 0, 5, 10, 20, 40, and 60 min and added to acetonitrile (5 × v:v, contains 10 ng/mL propranolol as internal standard) to stop the reaction and precipitate the protein. NADPH dependence of the reaction was evaluated with –NADPH samples. At the end of the assay, the samples were centrifuged through a Millipore Multiscreen Solvinert 0.45 μm low binding polytetrafluoroethylene (PTFE) hydrophilic filter plate and analyzed by liquid chromatography-tandem mass spectrometry (LC-MS/MS). Data were log-transformed and represented as half-lives.

Competitive ribosomal binding assay with [^{14}C]-erythromycin

A stock solution of *E. coli* ribosomes (20 nM, purified from MRE600 following literature precedent[31] and stored in a buffer solution containing 20 mM HEPES-KOH [pH 7.6], 6 mM $Mg(OAc)_2$, 50 mM NH_4OAc, and 4 mM β-mercaptoethanol) and [^{14}C]-erythromycin (20 nM, American Radiolabeled Chemicals) was prepared in binding buffer (1.5 mL per reaction, 20 mM Tris-HCl [pH 7.6], 10 mM $MgCl_2$, 150 mM NH_4Cl, and 6 mM β-mercaptoethanol) and incubated at 37°C for 30 min. 1.5 mL aliquots of this stock solution were dispensed into Eppendorf tubes, and CRM, C-CRM, O-CRM, or Se-CRM were added separately as solutions in DMSO (3 nM to 3,000 nM, 0.1% DMSO final concentration). The reactions were incubated for 1 h at 37°C. 20 μL of a manufacturer-supplied suspension (~50 mg/mL) of diethylaminoethyl (DEAE) magnetic beads (Bioclone #FM101), pre-washed with H_2O (1 × 1 mL) and binding buffer (2 × 1 mL), was added to each reaction. The resultant suspensions were incubated for an additional 15 min at 23°C. For each reaction, the beads were captured on a magnetic stand (Invitrogen), the supernatant was removed, and the beads were washed with ice-cold binding buffer (1 × 1 mL). 10 mM ethylenediaminetetraacetic acid (EDTA) solution (100 μL) was added to the beads and the resultant suspension was incubated for 10 min at 23°C to release bound [^{14}C]-erythromycin from the 70S ribosomes. The beads were re-captured on a magnetic stand and the eluent was transferred to scintillation vials containing 5 mL of liquid scintillation cocktail (PerkinElmer Ultima Gold). The radioactivity of each eluent solution was quantified by scintillation counting and the concentration of CRM, C-CRM, O-CRM, or Se-CRM at which half the bound radiolabeled erythromycin was displaced (IC_{50}) was determined using GraphPad Prism 10.0.2 software.

Primer extension inhibition (toeprinting) analysis

The primer extension inhibition (toeprinting) analysis of drug-dependent ribosome stalling was carried out using synthetic *ermDL* DNA template as previously described[32] with minor modifications. In brief, toeprinting reactions were carried out in 5-μL aliquots containing PURExpress transcription-translation coupled system (New England Biolabs, USA), to which the DNA template was added. The reactions were incubated at 37°C for 20–25 min. Reverse transcription on the templates was carried out using radioactively labeled primer NV1 (5′-GGTTATAAT-GAATTTTGCTTATTAAC-3′). Primer extension products were resolved on 6% denaturing sequencing gels. The final concentration of ERY, RET, CRM, O-CRM, C-CRM, or Se-CRM was 50 μM. In all reactions, we used 50 μM mupirocin (inhibitor of isoleucyl-tRNA synthetase) to arrest ribosomes at the Ile codon downstream of the macrolide arrest site (Figure S2).

X-ray crystallographic structure determination

Wild-type 70S ribosomes from *T. thermophilus* (strain HB8) were prepared as described previously.[21,22,33] Synthetic mRNA with the sequence 5′-GGC-AAG-GAG-GUA-AAA-AUG-UUC-UAA-3′ containing the Shine-Dalgarno sequence followed by the P-site methionine (AUG) and A-site phenylalanine (UUC) codons was obtained from Integrated DNA Technologies (Coralville, IA, USA). Ribosome complexes with mRNA and tRNAs were formed by incubating 5 μM *T. thermophilus* 70S ribosomes with 10 μM mRNA at 55°C for 10 min, followed by the addition of 20 μM fMet-$tRNA_i^{Met}$ and 20 μM deacylated $tRNA^{Phe}$ substrates.[10,22,34] For the ribosome complexes containing O-CRM, C-CRM, or Se-CRM, each compound was added to a final concentration of 100 μM, and the complexes were left at room temperature for an additional 15 min prior to crystallization. Ribosome complexes were prepared in the buffer containing 5 mM HEPES-KOH (pH 7.6), 50 mM KCl, 10 mM NH_4Cl, and 10 mM $Mg(OAc)_2$, and then crystallized in the buffer containing 100 mM Tris-HCl (pH 7.6), 2.9% (w/v) PEG-20,000, 9% (v/v)–10% (v/v) 2-methyl-2,4-pentanediol (MPD), 175 mM arginine, 0.5 mM β-mercaptoethanol. Crystals were grown by the vapor diffusion method in sitting drops at 19°C, then stabilized and cryo-protected stepwise using a series of buffers with increasing MPD concentrations (25%, 30%, and 35%) until reaching the final concentration of 40% (v/v) MPD as described previously.[10,22,34] The final 40% MPD stabilization buffer contained 100 μM of the corresponding compound. After stabilization, crystals were flash-frozen using a nitrogen cryo-stream at 80 K (Oxford Cryosystems, UK).

Collection and processing of the X-ray diffraction data, model building, and structure refinement were performed as previously described.[10,21,22,33,34] Diffraction data were collected at beamlines 24ID-C and 24ID-E at the Advanced Photon Source (Argonne National Laboratory). A complete dataset was collected using 0.979 Å X-ray irradiation at 100 K from multiple regions of the same crystal, using 0.3-degree oscillations. Raw data were integrated and scaled using the XDS software package (version from January 10, 2022).[35] Molecular replacement was performed using PHASER from the CCP4 program suite (version 7.0).[36] The search model was generated from the previously published structures of the *T. thermophilus* 70S ribosome with bound mRNA and aminoacylated tRNAs (PDB: 6XHW).[37] Initial molecular replacement solutions were refined by rigid-body refinement with the ribosome split into multiple domains, followed by positional and individual B-factor refinement using the PHENIX software (v.1.17).[38] Non-crystallographic symmetry restraints were applied to four parts of the 30S ribosomal subunit (head, body, spur, and helix 44) and four parts of the 50S subunit (body, L1-stalk, L10-stalk, and C terminus of the L9 protein). Initial PDB models and CIF restraints for O-CRM, C-CRM, or Se-CRM were generated using the PRODRG online software.[39] The final PDB model was built in Coot (v.0.8.2).[40] The statistics of data collection and refinement are compiled in Table S2. All figures showing atomic models were rendered using PyMOL Molecular Graphics System software (v.1.8.6, Schrödinger, www.pymol.org).

Computational methods

All EDA + DFT, and RI-MP2 calculations were run with Q-Chem 6.0.[23] The structures and locations of the ligand and binding pocket residues were extracted from the crystal structures via PyMOL.[41] Because our simulations only aim to describe the differences in interactions between CRM, C-CRM, O-CRM, and Se-CRM, we truncate the analogs by replacing their amide groups with hydrogen atoms. We truncate the G2505 residue by replacing the ribose sugar with a methyl group.

The truncated residues and CRM analogs were independently geometry-optimized at the ωB97X-V/def2-TZVPD level of theory and then repositioned to maximally align with the original structure using PyMol. For the interacting complex, only the positions of the hydrogen atoms were optimized, also at the ωB97X-V/def2-TZVPD level of theory. The orientations of the hydroxyl groups on the CRM analogs were selected based on geometry optimizations of a larger system containing the additional nearby nucleobase A2058 at the ωB97X-V/def2-SVPD level of theory. This demonstrated that the hydroxyl groups participate in intermolecular hydrogen bonds rather than intramolecular ones.

We evaluated the exchange-correlation potential and non-local correlation with the SG-2 and SG-1 quadrature grids respectively.[42,43] Following the literature,[44] we checked for grid dependence with the very dense (99, 590) and (50,194) grids for the exchange-correlation potential and non-local correlation, respectively. In the worst case (Se-CRM), the magnitude of the error introduced by a smaller grid is only 0.02, 0.07, 0.005, and 0.06 kcal/mol, respectively, for the interaction, frozen, polarization, and charge transfer energies. This provides confidence that the smaller grid is accurate.

While the DFT calculations conform with current best practices,[44,45] we additionally compared against RI-MP2, a computationally efficient *ab initio* approach,[46–48] and AFQMC, a quantum Monte Carlo method which has been demonstrated to provide gold-standard level accuracy in many classes of chemical systems while scaling to larger systems than CCSD(T) (Figure S6A).[26,49–51] The calculations performed here provide a potential template for future drug discovery applications for molecules with stronger electronic correlation.[52,53]

The DFT results are in excellent agreement with the AFQMC results while MP2 overshoots the interaction energy, which is expected.[54,55] AFQMC distinguishes O-CRM and Se-CRM as the weakest and strongest interactions, respectively, but does not resolve the ordering between CRM and C-CRM. These results do confirm, however, that DFT is an appropriate choice of methodology for further analysis.

EDA and polarizable continuum model (PCM) calculations were carried out following literature precedent[44] and at the ωB97X-V/def2-TZVPD level of theory. All interaction energies are corrected for basis set superposition error via a counterpoise correction. The solvent accessible surface for PCM was generated with a 1.4 Å solvent probe radius and the results were basis set superposition error (BSSE) corrected by using the BSSE correction from the gas phase calculation. We considered the effect of solvents with varying dielectric constants (Figure S6B); increasing the continuum dielectric constant lowers the interaction energy for CRM, O-CRM, and Se-CRM, while the interaction energy for C-CRM remains nearly constant. This suggests that in the full rRNA environment, C-CRM will have a weaker binding affinity than CRM, consistent with the experiments; however, direct calculations of binding free energies differences would be required for a more quantitative statement.[56,57]

The RI-MP2 calculations were performed on each system using the cc-pVTZ and cc-pVQZ basis sets and corresponding auxiliary basis sets.[58–60] The complete basis set (CBS) result was extracted via a two-point extrapolation of the RI-MP2 correlation energy from the following formula:

$$(E_{\mathrm{RI-MP2}})_{\mathrm{CBS}} = (E_{\mathrm{HF}})_{\mathrm{QZ}} \mp \frac{\left((E_{corr\ \mathrm{RI-MP2}})_{\mathrm{QZ}}\, 4^3 - (E_{corr\ \mathrm{RI-MP2}})_{\mathrm{TZ}}\, 3^3\right)}{4^3 - 3^3} \qquad \text{(Equation 1)}$$

The AFQMC calculations were performed with ipie[26,61] using restricted Hartree-Fock (RHF) trials generated by PySCF.[62] The Cholesky decomposition of the two electron integrals was found to introduce a minimal amount of error with a cutoff of 10^{-4} for C-CRM and O-CRM and 10^{-5} for CRM and Se-CRM. Because AFQMC calculations are computationally demanding, we approximate the CBS correction for AFQMC at the cc-pVTZ level with the RI-MP2 CBS extrapolation energy using the following formula:

$$(E_{\mathrm{AFQMC}})_{\mathrm{CBS}} = (E_{\mathrm{AFQMC}})_{\mathrm{TZ}} \mp \left((E_{\mathrm{RI-MP2}})_{\mathrm{CBS}} - (E_{\mathrm{RI-MP2}})_{\mathrm{TZ}}\right) \qquad \text{(Equation 2)}$$

RESOURCE AVAILABILITY

Lead contact

Requests for further information and resources should be directed to and will be fulfilled by the lead contact, Prof. Andrew G. Myers (myers@chemistry.harvard.edu).

Materials availability

All reagents and solvents used in this study were purchased from commercial sources and used as received.

Data and code availability

All data supporting the findings of this study are presented within the article and supplemental information. Coordinates and structure factors were deposited in the Research Collaboratory for Structural Bioinformatics (RCSB) Protein Data Bank (PDB) with the following accession codes: PDB: **9D0G** for the wild-type *T. thermophilus* 70S ribosome in complex with O-CRM, mRNA, deacylated A-site tRNA$^{\mathrm{Phe}}$, aminoacylated P-site fMet-tRNA$_{\mathrm{i}}^{\mathrm{Met}}$, and deacylated E-site tRNA$^{\mathrm{Phe}}$; PDB: **9D0H** for the wild-type *T. thermophilus* 70S ribosome in complex with C-CRM, mRNA, deacylated A-site tRNA$^{\mathrm{Phe}}$, aminoacylated P-site fMet-tRNA$_{\mathrm{i}}^{\mathrm{Met}}$, and deacylated E-site tRNA$^{\mathrm{Phe}}$; PDB: **9D0I** for the wild-type *T. thermophilus* 70S ribosome in complex with Se-CRM, mRNA, deacylated A-site tRNA$^{\mathrm{Phe}}$, aminoacylated P-site fMet-tRNA$_{\mathrm{i}}^{\mathrm{Met}}$, and deacylated E-site tRNA$^{\mathrm{Phe}}$. All previously published structures that were used in this work for structural comparisons were retrieved from the RCSB PDB: 8UD6.

ACKNOWLEDGMENTS

We thank Dr. Michael Cameron for the collection of liver microsomal stability data. We thank the staff at NE-CAT beamlines 24ID-C and 24ID-E for help with X-ray diffraction data collection, especially Drs. Malcolm Capel, Frank Murphy, Surajit Banerjee, Igor Kourinov, David Neau, Jonathan Schuermann, Narayanasami Sukumar, Anthony Lynch, James Withrow, Kay Perry, Ali Kaya, and Cyndi Salbego. We thank Dr. Alexander Mankin and Dr. Mark Brönstrup for their invaluable insights over the course of our research. This work is based upon research conducted at the Northeastern Collaborative Access Team beamlines, which are funded by the National Institute of General Medical Sciences from the National Institutes of Health (P30-GM124165 to NE-CAT). The Eiger 16M detector on 24-ID-E beamline is funded by an NIH-ORIP HEI grant (S10-OD021527 to NE-CAT). This research used the resources of the Advanced Photon Source, a US Department of Energy (DOE) Office of Science User Facility operated for the DOE Office of Science by Argonne National Laboratory under contract no. DE-AC02-06CH11357. This work was supported by the National Institute of Allergy and Infectious Diseases of the National Institutes of Health (R01-AI168228 to A.G.M. and R21-AI163466 to Y.S.P.), National Institute of General Medical Sciences of the National Institutes of Health (R01-GM132302 and R35-GM151957 to Y.S.P.), the Illinois State startup funds (to Y.S.P.), National Science Foundation (MCB-2345351 to M.S.S.), the Arnold O. Beckman Postdoctoral Fellowship in Chemical Sciences (to P.J.R.), the William F. Milton Fund (to J.L.), Wellcome Leap's Supported Challenge Program in Quantum for Bio (to P.J.R., T.J., and J.L.). The funders had no role in study design, data collection and analysis, decision to publish, or manuscript preparation.

AUTHOR CONTRIBUTIONS

K.J.Y.W., A.E.B., M.Y., B.I.C.T., and D.N.Y.S. synthesized CRM, O-CRM, C-CRM, and Se-CRM; A.R. performed microbiological assays; B.I.C.T. and M.S.S. performed *in vitro* competition binding assays; C.F.D. and M.S.S. performed *in vitro* toeprinting assays; E.V.A. prepared hydrolysis-resistant aminoacyl tRNAs; E.V.A. and Y.S.P. designed and performed X-ray crystallography experiments; P.J.R. designed and performed DFT calculations; T.J. designed and performed AFQMC calculations; K.J.Y.W. conceptualized the work; J.L. supervised the theoretical work; A.G.M. and Y.S.P. supervised the experiments. All authors interpreted the results. K.J.Y.W., Y.S.P., and A.G.M. wrote the manuscript.

DECLARATION OF INTERESTS

K.J.Y.W., B.I.C.T., and A.G.M. are shareholders of Kinvard Bio Inc., and have filed international patent application WO/2023/205206, "Lincosamides and Uses Thereof."

SUPPLEMENTAL INFORMATION

Supplemental information can be found online at https://doi.org/10.1016/j.chempr.2025.102480.

Received: December 2, 2024
Revised: January 15, 2025
Accepted: February 7, 2025
Published: March 7, 2025

REFERENCES

1. Wilson, D.N. (2014). Ribosome-targeting antibiotics and mechanisms of bacterial resistance. Nat. Rev. Microbiol. *12*, 35–48. https://doi.org/10.1038/nrmicro3155.
2. Lin, J., Zhou, D., Steitz, T.A., Polikanov, Y.S., and Gagnon, M.G. (2018). Ribosome-targeting antibiotics: modes of action, mechanisms of resistance, and implications for drug design. Annu. Rev. Biochem. *87*, 451–478. https://doi.org/10.1146/annurev-biochem-062917-011942.
3. Schlünzen, F., Zarivach, R., Harms, J., Bashan, A., Tocilj, A., Albrecht, R., Yonath, A., and Franceschi, F. (2001). Structural basis for the interaction of antibiotics with the peptidyl transferase centre in eubacteria. Nature *6858*, 814–821. https://doi.org/10.1038/35101544.
4. MacLeod, A.J., Ross, H.B., Ozere, R.L., Digout, G., and Van Rooyen, C.E. (1964). Lincomycin: A new antibiotic active against staphylococci and other Gram-positive cocci: clinical and laboratory studies. Can. Med. Assoc. J. *91*, 1056–1060.
5. Birkenmeyer, R.D., and Kagan, F. (1970). Lincomycin. XI. Synthesis and structure of clindamycin. A potent antibacterial agent. J. Med. Chem. *13*, 616–619. https://doi.org/10.1021/jm00298a007.
6. Brodasky, T.F., Lewis, C., and Eble, T.E. (1977). Distribution and metabolism of antibiotics in the whole animal I. Clindamycin in the rat. Eur. J. Drug Metab. Pharmacokinet. *2*, 149–156. https://doi.org/10.1007/BF03189299.
7. Wynalda, M.A., Hutzler, J.M., Koets, M.D., Podoll, T., and Wienkers, L.C. (2003). In vitro metabolism of clindamycin in human liver and intestinal microsomes. Drug Metab. Dispos. *31*, 878–887. https://doi.org/10.1124/dmd.31.7.878.
8. Lewis, J.G., Anandan, S.K., O'Dowd, H., Gordeev, M.F., and Li, L. (2008). Lincomycin derivatives possessing antibacterial activity. US Patent 7,361,743B2.
9. Mitcheltree, M.J., Stevenson, J.W., Pisipati, A., and Myers, A.G. (2021). A practical, component-based synthetic route to Methylthiolincosamine

permitting facile northern-half diversification of lincosamide antibiotics. J. Am. Chem. Soc. *143*, 6829–6835. https://doi.org/10.1021/jacs.1c03536.

10. Wu, K.J.Y., Tresco, B.I.C., Ramkissoon, A., Aleksandrova, E.V., Syroegin, E.A., See, D.N.Y., Liow, P., Dittemore, G.A., Yu, M., Testolin, G., et al. (2024). An antibiotic preorganized for ribosomal binding overcomes antimicrobial resistance. Science *383*, 721–726. https://doi.org/10.1126/science.adk8013.
11. Doyle, L.M., O'Sullivan, S., Di Salvo, C., McKinney, M., McArdle, P., and Murphy, P.V. (2017). Stereoselective epimerizations of glycosyl thiols. Org. Lett. *19*, 5802–5805. https://doi.org/10.1021/acs.orglett.7b02760.
12. Giannis, A., and Sandhoff, K. (1985). Stereoselective synthesis of α-C-allyl-glycopyranosides. Tetrahedron Lett. *26*, 1479–1482. https://doi.org/10.1016/S0040-4039(00)98529-0.
13. Bhat, A.S., and Gervay-Hague, J. (2001). Efficient Syntheses of β-Cyanosugars Using glycosyl Iodides Derived from Per- *O* -silylated Mono- and Disaccharides. Org. Lett. *3*, 2081–2084. https://doi.org/10.1021/ol0160405.
14. Du, W., and Gervay-Hague, J. (2005). Efficient synthesis of α-galactosyl ceramide analogues using glycosyl iodide donors. Org. Lett. *7*, 2063–2065. https://doi.org/10.1021/ol050659f.
15. Nanami, M., Ando, H., Kawai, Y., Koketsu, M., and Ishihara, H. (2007). Stereoselective synthesis of various α-selenoglycosides using in situ production of α-selenolate anion. Tetrahedron Lett. *48*, 1113–1116. https://doi.org/10.1016/J.TETLET.2006.12.056.
16. Mason, J.D., Terwilliger, D.W., Pote, A.R., and Myers, A.G. (2021). Practical gram-scale synthesis of Iboxamycin, a potent antibiotic candidate. J. Am. Chem. Soc. *143*, 11019–11025. https://doi.org/10.1021/JACS.1C03529.
17. Wu K.J.Y., Liow P., Myers A.G. (2025). Practical Synthesis of Oxepanoprolines. Org. Process Res. Dev. Article ASAP. https://doi.org/10.1021/acs.oprd.4c00521.
18. Hartz, D., McPheeters, D.S., Traut, R., and Gold, L. (1988). Extension inhibition analysis of translation initiation complexes. Methods Enzymol. *164*, 419–425. https://doi.org/10.1016/S0076-6879(88)64058-4.
19. Myers, A.G., and Clark, R.B. (2021). Discovery of macrolide antibiotics effective against multi-drug resistant Gram-negative pathogens. Acc. Chem. Res. *54*, 1635–1645. https://doi.org/10.1021/acs.accounts.1c00020.
20. Svetlov, M.S., Vázquez-Laslop, N., and Mankin, A.S. (2017). Kinetics of drug-ribosome interactions defines the cidality of macrolide antibiotics. Proc. Natl. Acad. Sci. USA *114*, 13673–13678. https://doi.org/10.1073/pnas.1717168115.
21. Polikanov, Y.S., Steitz, T.A., and Innis, C.A. (2014). A proton wire to couple aminoacyl-tRNA accommodation and peptide-bond formation on the ribosome. Nat. Struct. Mol. Biol. *21*, 787–793. https://doi.org/10.1038/nsmb.2871.
22. Polikanov, Y.S., Melnikov, S.V., Söll, D., and Steitz, T.A. (2015). Structural insights into the role of rRNA modifications in protein synthesis and ribosome assembly. Nat. Struct. Mol. Biol. *22*, 342–344. https://doi.org/10.1038/nsmb.2992.
23. Epifanovsky, E., Gilbert, A.T.B., Feng, X., Lee, J., Mao, Y., Mardirossian, N., Pokhilko, P., White, A.F., Coons, M.P., Dempwolff, A.L., et al. (2021). Software for the frontiers of quantum chemistry: an overview of developments in the Q-Chem 5 package. J. Chem. Phys. *155*, 084801. https://doi.org/10.1063/5.0055522.
24. Cuervo, A., Dans, P.D., Carrascosa, J.L., Orozco, M., Gomila, G., and Fumagalli, L. (2014). Direct measurement of the dielectric polarization properties of DNA. Proc. Natl. Acad. Sci. USA *111*, E3624–E3630. https://doi.org/10.1073/pnas.1405702111.
25. Zhang, S., and Krakauer, H. (2003). Quantum Monte Carlo method using phase-free random walks with slater determinants. Phys. Rev. Lett. *90*, 136401. https://doi.org/10.1103/PhysRevLett.90.136401.
26. Jiang, T., Baumgarten, M.K.A., Loos, P.-F., Mahajan, A., Scemama, A., Ung, S.F., Zhang, J., Malone, F.D., and Lee, J. (2024). Improved modularity and new features in ipie: toward even larger AFQMC calculations on CPUs and GPUs at zero and finite temperatures. J. Chem. Phys. *161*, 162502. https://doi.org/10.1063/5.0225596.
27. Hoeksema, H. (1964). Celesticetin. IV. The structure of celesticetin. J. Am. Chem. Soc. *86*, 4224–4225. https://doi.org/10.1021/ja01073a084.
28. Birkenmeyer, R.D., Kroll, S.J., Lewis, C., Stern, K.F., and Zurenko, G.E. (1984). Synthesis and antimicrobial activity of clindamycin analogues: pirlimycin, a potent antibacterial agent. J. Med. Chem. *27*, 216–223. https://doi.org/10.1021/JM00368A020/ASSET/JM00368A020.FP.PNG_V03.
29. Tresco, B.I.C., Wu, K.J.Y., Ramkissoon, A., Aleksandrova, E.V., Purdy, M., See, D.N.Y., Liu, R.Y., Polikanov, Y.S., and Myers, A.G. (2025). Discovery of a Fluorinated Macrobicyclic Antibiotic through Chemical Synthesis. Nat. Chem. In press. https://doi.org/10.1038/s41557-025-01738-7.3.
30. Clinical and Laboratory Standards Institute (CLSI) (2023). Performance Standards for Antimicrobial Susceptibility Testing, Thirty-Third Edition (CLSI).
31. Shimizu, Y., Inoue, A., Tomari, Y., Suzuki, T., Yokogawa, T., Nishikawa, K., and Ueda, T. (2001). Cell-free translation reconstituted with purified components. Nat. Biotechnol. *19*, 751–755. https://doi.org/10.1038/90802.
32. Chen, C.-W., Leimer, N., Syroegin, E.A., Dunand, C., Bulman, Z.P., Lewis, K., Polikanov, Y.S., and Svetlov, M.S. (2023). Structural insights into the mechanism of overcoming Erm-mediated resistance by macrolides acting together with hygromycin-A. Nat. Commun. *14*, 4196. https://doi.org/10.1038/s41467-023-39653-5.
33. Syroegin, E.A., Aleksandrova, E.V., and Polikanov, Y.S. (2023). Insights into the ribosome function from the structures of non-arrested ribosome–nascent chain complexes. Nat. Chem. *15*, 143–153. https://doi.org/10.1038/s41557-022-01073-1.
34. Mitcheltree, M.J., Pisipati, A., Syroegin, E.A., Silvestre, K.J., Klepacki, D., Mason, J.D., Terwilliger, D.W., Testolin, G., Pote, A.R., Wu, K.J.Y., et al. (2021). A synthetic antibiotic class overcoming bacterial multidrug resistance. Nature *7885*, 507–512. https://doi.org/10.1038/s41586-021-04045-6.
35. Kabsch, W. (2010). XDS. Acta Crystallogr. D Biol. Crystallogr. *66*, 125–132. https://doi.org/10.1107/S0907444909047337.
36. McCoy, A.J., Grosse-Kunstleve, R.W., Adams, P.D., Winn, M.D., Storoni, L.C., and Read, R.J. (2007). *Phaser* crystallographic software. J. Appl. Crystallogr. *40*, 658–674. https://doi.org/10.1107/S0021889807021206.
37. Svetlov, M.S., Syroegin, E.A., Aleksandrova, E.V., Atkinson, G.C., Gregory, S.T., Mankin, A.S., and Polikanov, Y.S. (2021). Structure of Erm-modified 70S ribosome reveals the mechanism of macrolide resistance. Nat. Chem. Biol. *17*, 412–420. https://doi.org/10.1038/s41589-020-00715-0.
38. Adams, P.D., Afonine, P.V., Bunkóczi, G., Chen, V.B., Davis, I.W., Echols, N., Headd, J.J., Hung, L.-W., Kapral, G.J., Grosse-Kunstleve, R.W., et al. (2010). *Phenix*: a comprehensive Python-based system for macromolecular structure solution. Acta Crystallogr. D Biol. Crystallogr. *66*, 213–221. https://doi.org/10.1107/S0907444909052925.
39. Schüttelkopf, A.W., and van Aalten, D.M.F. (2004). *PRODRG*: a tool for high-throughput crystallography of protein–ligand complexes. Acta Crystallogr. D Biol. Crystallogr. *60*, 1355–1363. https://doi.org/10.1107/S0907444904011679.
40. Emsley, P., and Cowtan, K. (2004). *Coot*: model-building tools for molecular graphics. Acta Crystallogr. D Biol. Crystallogr. *60*, 2126–2132. https://doi.org/10.1107/S0907444904019158.
41. Schrödinger LLC (2015). In The PyMOL Molecular Graphics System, Version 2.5.8 (Schrödinger, LLC).
42. Gill, P.M.W., Johnson, B.G., and Pople, J.A. (1993). A standard grid for density functional calculations. Chem. Phys. Lett. *209*, 506–512. https://doi.org/10.1016/0009-2614(93)80125-9.

43. Dasgupta, S., and Herbert, J.M. (2017). Standard grids for high-precision integration of modern density functionals: SG-2 and SG-3. J. Comput. Chem. *38*, 869–882. https://doi.org/10.1002/jcc.24761.
44. Carter-Fenk, K., Liu, M., Pujal, L., Loipersberger, M., Tsanai, M., Vernon, R.M., Forman-Kay, J.D., Head-Gordon, M., Heidar-Zadeh, F., and Head-Gordon, T. (2023). The energetic origins of pi–pi contacts in proteins. J. Am. Chem. Soc. *145*, 24836–24851. https://doi.org/10.1021/jacs.3c09198.
45. Mardirossian, N., and Head-Gordon, M. (2014). ωB97X-V: A 10-parameter, range-separated hybrid, generalized gradient approximation density functional with nonlocal correlation, designed by a survival-of-the-fittest strategy. Phys. Chem. Chem. Phys. *16*, 9904–9924. https://doi.org/10.1039/c3cp54374a.
46. Feyereisen, M., Fitzgerald, G., and Komornicki, A. (1993). Use of approximate integrals in ab initio theory. An application in MP2 energy calculations. Chem. Phys. Lett. *208*, 359–363. https://doi.org/10.1016/0009-2614(93)87156-W.
47. Dunlap, B.I. (2000). Robust and variational fitting. Phys. Chem. Chem. Phys. *2*, 2113–2116. https://doi.org/10.1039/B000027M.
48. Jung, Y., Sodt, A., Gill, P.M.W., and Head-Gordon, M. (2005). Auxiliary basis expansions for large-scale electronic structure calculations. Proc. Natl. Acad. Sci. USA *102*, 6692–6697. https://doi.org/10.1073/pnas.0408475102.
49. Lee, J., Pham, H.Q., and Reichman, D.R. (2022). Twenty years of auxiliary-field quantum Monte Carlo in quantum chemistry: an overview and assessment on main group chemistry and bond-breaking. J. Chem. Theor. Comput. *18*, 7024–7042. https://doi.org/10.1021/acs.jctc.2c00802.
50. Shee, J., Weber, J.L., Reichman, D.R., Friesner, R.A., and Zhang, S. (2023). On the potentially transformative role of auxiliary-field quantum Monte Carlo in quantum chemistry: A highly accurate method for transition metals and beyond. J. Chem. Phys. *158*, 140901. https://doi.org/10.1063/5.0134009.
51. Wei, Y., Debnath, S., Weber, J.L., Mahajan, A., Reichman, D.R., and Friesner, R.A. (2024). Scalable ab initio electronic structure methods with near chemical accuracy for main group chemistry. J. Phys. Chem. A *128*, 5796–5807. https://doi.org/10.1021/acs.jpca.4c02853.
52. Huggins, W.J., O'Gorman, B.A., Rubin, N.C., Reichman, D.R., Babbush, R., and Lee, J. (2022). Unbiasing fermionic quantum Monte Carlo with a quantum computer. Nature *603*, 416–420. https://doi.org/10.1038/s41586-021-04351-z.
53. Santagati, R., Aspuru-Guzik, A., Babbush, R., Degroote, M., González, L., Kyoseva, E., Moll, N., Oppel, M., Parrish, R.M., Rubin, N.C., et al. (2024). Drug design on quantum computers. Nat. Phys. *20*, 549–557. https://doi.org/10.1038/s41567-024-02411-5.
54. Ballesteros, F., Dunivan, S., and Lao, K.U. (2021). Coupled cluster benchmarks of large noncovalent complexes: the L7 dataset as well as DNA–ellipticine and buckycatcher–fullerene. J. Chem. Phys. *154*, 154104. https://doi.org/10.1063/5.0042906.
55. Al-Hamdani, Y.S., Nagy, P.R., Zen, A., Barton, D., Kállay, M., Brandenburg, J.G., and Tkatchenko, A. (2021). Interactions between large molecules pose a puzzle for reference quantum mechanical methods. Nat. Commun. *12*, 3927. https://doi.org/10.1038/s41467-021-24119-3.
56. Brandsdal, B.O., Österberg, F., Almlöf, M., Feierberg, I., Luzhkov, V.B., and Åqvist, J. (2003). Free energy calculations and ligand binding. In Advances in Protein Chemistry, *66* (Academic Press), pp. 123–158. https://doi.org/10.1016/S0065-3233(03)66004-3.
57. Cournia, Z., Allen, B., and Sherman, W. (2017). Relative binding free energy calculations in drug discovery: recent advances and practical considerations. J. Chem. Inf. Model. *57*, 2911–2937. https://doi.org/10.1021/acs.jcim.7b00564.
58. Dunning, T.H., Jr. (1989). Gaussian basis sets for use in correlated molecular calculations. I. The atoms boron through neon and hydrogen. J. Chem. Phys. *90*, 1007–1023. https://doi.org/10.1063/1.456153.
59. Woon, D.E., and Dunning, T.H., Jr. (1993). Gaussian basis sets for use in correlated molecular calculations. III. The atoms aluminum through argon. J. Chem. Phys. *98*, 1358–1371. https://doi.org/10.1063/1.464303.
60. Wilson, A.K., Woon, D.E., Peterson, K.A., and Dunning, T.H., Jr. (1999). Gaussian basis sets for use in correlated molecular calculations. IX. The atoms gallium through krypton. J. Chem. Phys. *110*, 7667–7676. https://doi.org/10.1063/1.478678.
61. Malone, F.D., Mahajan, A., Spencer, J.S., and Lee, J. (2023). ipie: A Python-Based Auxiliary-Field Quantum Monte Carlo Program with Flexibility and Efficiency on CPUs and GPUs. J. Chem. Theor. Comput. *19*, 109–121. https://doi.org/10.1021/acs.jctc.2c00934.
62. Sun, Q., Zhang, X., Banerjee, S., Bao, P., Barbry, M., Blunt, N.S., Bogdanov, N.A., Booth, G.H., Chen, J., Cui, Z.-H., et al. (2020). Recent developments in the PySCF program package. J. Chem. Phys. *153*, 024109. https://doi.org/10.1063/5.0006074.